



# Boosting the adsorption and photocatalytic activity of carbon fiber/ MoS<sub>2</sub>-based weavable photocatalyst by decorating UiO-66-NH<sub>2</sub> nanoparticles

Wei Cao<sup>a,b,1</sup>, Yan Zhang<sup>a,b,1</sup>, Zhun Shi<sup>a</sup>, Ting Liu<sup>a</sup>, Xinshan Song<sup>a</sup>, Lisha Zhang<sup>a,b,\*</sup>,  
Po Keung Wong<sup>d,e</sup>, Zhigang Chen<sup>c,\*</sup>

<sup>a</sup> State Key Laboratory for Modification of Chemical Fibers and Polymer Materials, State Environmental Protection Engineering Center for Pollution Treatment and Control in Textile Industry, College of Environmental Science and Engineering, Donghua University, Shanghai 201620, China

<sup>b</sup> Shanghai Institute of Pollution Control and Ecological Security, Shanghai 200092, China

<sup>c</sup> International Joint Laboratory for Advanced Fiber and Low Dimension Materials, College of Materials Science and Engineering, Donghua University, Shanghai 201620, China

<sup>d</sup> School of Life Sciences, The Chinese University of Hong Kong, Shatin, NT, Hong Kong

<sup>e</sup> Institute of Environmental Health and Pollution Control, School of Environmental Science & Engineering, Guangdong University of Technology, Guangzhou 510006, China

## ARTICLE INFO

### Keywords:

MoS<sub>2</sub>/UiO-66-NH<sub>2</sub>  
Carbon fiber  
Weavable photocatalyst  
Levofloxacin  
Visible light

## ABSTRACT

MoS<sub>2</sub>-based nanocomposites on carbon fibers (CFs) have been well developed, but their practical applications are still limited owing to the unsatisfactory adsorption and photodegradation performances. To deal with these issues, we report the growth of UiO-66-NH<sub>2</sub> nanoparticles as a porous co-photocatalyst to decorate MoS<sub>2</sub> nanosheets on CFs. CFs/MoS<sub>2</sub>/UiO-66-NH<sub>2</sub> bundles are woven into a macroscopical cloth (4 × 4 cm<sup>2</sup>, 0.15 g). CFs/MoS<sub>2</sub>/UiO-66-NH<sub>2</sub> cloth can efficiently adsorb 34.9% levofloxacin (LVFX) and 35.3% hexavalent chromium (Cr(VI)) after 60 min, which is an obvious improvement (1.3–2.9 times) compared with that by CFs/MoS<sub>2</sub> cloth. Importantly, the cloth can remove 88.4% LVFX or 98.4% Cr(VI) within 120 min, which is 1.6–2.7 times compared with that by CFs/MoS<sub>2</sub> cloth, resulting from the high adsorption and two-component synergistic photocatalytic activity. Furthermore, CFs/MoS<sub>2</sub>/UiO-66-NH<sub>2</sub> shows a slight decline from 88.4% to 76.9% under visible light irradiation after 4 cycles. Thus, the semiconductor/MOF-based heterojunction on CF provides a general strategy to develop novel weavable photocatalysts for eliminating various pollutants.

## 1. Introduction

With the development of the industrial enterprises, lots of wastewater has been released to the river and other water bodies. There are huge challenges in treating the wastewater, which contains organic pollutants (including dyes, herbicides, antibiotics) or heavy metal ions (including Cr(VI)), due to their recalcitrance and persistence [1]. To effectively remove the aqueous organic pollutants and heavy metal ions, many techniques have been well developed, such as advanced oxidation technology [2], biodegradation [3], electrocatalysis [4], membrane separation [5], and photocatalytic technology [6]. Among them, photocatalysis is an ideal strategy because of the low toxicity, low energy-

consumption, high efficiency and mild reaction condition [7]. The key issue is to prepare efficient and cost-effective photocatalysts [8]. Many photocatalysts have been constructed, for instance, oxides (TiO<sub>2</sub> [9], Mn<sub>2</sub>O<sub>3</sub> [10]), sulfides (MoS<sub>2</sub> [11], ZnS [12]) and nitrides (g-C<sub>3</sub>N<sub>4</sub> [13]). Among them, MoS<sub>2</sub> as a two-dimensional (2D) layered material is an excellent candidate for photocatalytic application due to the abundant active sites and wide-spectrum response. For example, Adhikari et al. fabricated MoS<sub>2</sub>/Ag<sub>2</sub>Mo<sub>2</sub>O<sub>7</sub> nanomaterials, which could degrade 97% LVFX in 120 min under visible-light irradiation [14]. Besides, 110-BiOBr could remove 54.5% Cr(VI) in 120 min under visible-light irradiation [15]. Although these powder-shaped materials exhibit high photocatalytic activity, they are limited in practical application due to the

\* Corresponding authors at: State Key Laboratory for Modification of Chemical Fibers and Polymer Materials, State Environmental Protection Engineering Center for Pollution Treatment and Control in Textile Industry, College of Environmental Science and Engineering, Donghua University, Shanghai 201620, China (L. Zhang).

E-mail addresses: [lszhang@dhu.edu.cn](mailto:lszhang@dhu.edu.cn) (L. Zhang), [zgchen@dhu.edu.cn](mailto:zgchen@dhu.edu.cn) (Z. Chen).

<sup>1</sup> These authors contributed equally to this work.

difficulty of recycling. Therefore, it is urgent to immobilize nanoparticles for purifying wastewater.

To fix these nanostructured photocatalysts, three methods have been widely developed. The first is fabricating nanomaterials on flat substrates such as indium tin oxide (ITO) glass or metal foil [16]. For instance,  $\text{SnO}_2/\text{Zn}_2\text{SnO}_4$  composite was prepared on stainless steel mesh, and it could degrade 89.8% methyl orange (MO) within 150 min of simulated sunlight illumination [17]. Photocatalysts on flat substrates can be easily recycled, but they possess low surface area/flexibility and high cost. The second strategy is constructing semiconductor nonwoven cloths with nanostructured materials via electrospinning-based routes. For example, our group has reported the preparation of  $\text{Fe}_2\text{O}_3/\text{AgBr}$  [18] and  $\text{Ta}_3\text{N}_5/\text{Pt}$  nonwoven cloth [19], and these nonwoven cloths exhibit superior ability for removing contaminants. It should be noted that these nonwoven cloths are fragile and thus it is difficult to obtain cloths with large area. The last one is constructing semiconductor nanomaterials on flexible fibers or fabrics [6]. Among them, carbon fiber (CF) is a promising material due to its laudable conductivity, pliability and mechanical intensity [20]. For example,  $\text{CFs}/\text{MoS}_2/\text{Bi}_2\text{S}_3$  can adsorb (24.4%) and degrade (74.5%) TC in 100 min under visible-light irradiation [21]. However, resulting from the high proportion of CF which shows a low specific surface area, the as-prepared photocatalysts may display insufficient synergy between adsorption and degradation for the rapid removal of pollutants. Therefore, it is still essential to fabricate photocatalysts with superior adsorption and degradation efficiency.

Metal-organic frameworks (MOFs) have a large specific surface area, controllable pore architecture, unique physicochemical properties, adjustability and variability of structures [22]. Since MOF-5 was demonstrated to have semiconductor behavior to photocatalytically degrade phenol in 2007 for the first time [23], many kinds of semiconductor-like MOFs (such as MIL-125, UiO-66 and MIL-53) have been well developed as co-photocatalysts. Among these MOF-based co-photocatalysts, Zr-based MOFs are preferable due to excellent thermal and chemical stability. As the typical Zr-based MOFs, UiO-66 is attracting the increasing attention in the photocatalytic field, due to its semiconductor properties and excellent physical/chemical properties [24]. Moreover, if UiO-66 is modified by amino functional-groups, UiO-66-NH<sub>2</sub> can work as a visible-light-driven catalyst. Wang et al. prepared Pd@UiO-66-NH<sub>2</sub> metal-organic framework, and the Pd@UiO-66-NH<sub>2</sub> could degrade 99% Cr(VI) within 90 min under visible light irradiation [25]. AgI/UiO-66-NH<sub>2</sub> heterojunction could degrade 80.7% tetracycline (TC) after 40 min under visible-light irradiation [26]. Unfortunately, these MOFs materials are also powder-shaped, and they cannot be efficiently recycled in practical applications.

To further improve the adsorption and photocatalytic activity of weavable CF/MoS<sub>2</sub>-based photocatalysts and to address the recycling difficulty of MOFs-based photocatalysts, we proposed the surface decoration of CF/MoS<sub>2</sub> with UiO-66-NH<sub>2</sub> as porous co-photocatalysts. CFs/MoS<sub>2</sub>/UiO-66-NH<sub>2</sub> bundles displayed a wide absorption in 200–800 nm with an edge (~470 nm). The obtained bundles could be further weaved into a macroscopical cloth (0.15 g, 4 × 4 cm<sup>2</sup>). The adsorption and photocatalytic activities of the cloth were investigated, and the effects of pH/pollutant concentration/inorganic ions were analyzed. CFs/MoS<sub>2</sub>/UiO-66-NH<sub>2</sub> cloth exhibited the highest adsorption and two-component synergistic photocatalytic capacity for degrading LVFX and Cr(VI), with high recyclability and stability.

## 2. Experimental section

### 2.1. Material synthesis

#### 2.1.1. Synthesis of CFs/MoS<sub>2</sub>

The treatment of CFs is shown in Electronic Supporting Information (ESI). MoS<sub>2</sub> nanosheets on CFs was prepared by a modified hydrothermal route [27]. In a typical process, (NH<sub>4</sub>)<sub>6</sub>Mo<sub>7</sub>O<sub>24</sub>·4H<sub>2</sub>O (2 mmol) and

CH<sub>4</sub>N<sub>2</sub>S (30 mmol) were added in the aqueous solution (70 mL) containing CFs at 200 °C for 24 h. The obtained CFs/MoS<sub>2</sub> was washed three times with ethanol and water, and dried (60 °C 12 h).

#### 2.1.2. Synthesis of CFs/MoS<sub>2</sub>/UiO-66-NH<sub>2</sub>

CFs/MoS<sub>2</sub>/UiO-66-NH<sub>2</sub> were prepared by a modified solvothermal method [28]. ZrCl<sub>4</sub> (0.8 mmol) and 2-aminoterephthalic acid (0.8 mmol) were added in DMF (81.7 mL). Subsequently, acetic acid (4.6 g) was dissolved into the above mixed solution. The above solution was put into a stainless-steel autoclave together with CFs/MoS<sub>2</sub>. Then, the autoclave was sealed and solvothermal treated (120 °C 24 h). Finally, these fibers were taken out and washed by DMF and ethanol, and dried (60 °C 12 h).

### 2.2. Measurements of adsorption and photocatalytic activity

CFs/MoS<sub>2</sub>/UiO-66-NH<sub>2</sub> bundles (weight: 0.15 g, length: 4 cm) were divided into several bundles equally, and these bundles are interlaced or hooked together by hand-knitting to obtain CFs/MoS<sub>2</sub>/UiO-66-NH<sub>2</sub> cloth. For comparison, other different flexible bundles (CFs, CFs/MoS<sub>2</sub> and CFs/UiO-66-NH<sub>2</sub>) were reorganized and woven into cloths (4 × 4 cm<sup>2</sup>, ~0.15 g). The adsorption and photocatalytic activity of these cloths were tested by removing LVFX (20 mg/L, 100 mL) and Cr(VI) (50 mg/L, 100 mL) as models of pollutants. In the dark, the as-prepared cloths were immersed in the solution for 60 min to explore the adsorption capacity. Then the solution with as-prepared cloths was irradiated by visible-light (Beijing Perfectlight Co. Ltd., PLS-SXE300D, 300 W, 15 A) to measure the photocatalytic efficiency. Besides, the effects of pH, LVFX concentration, inorganic ions, radical trapping tests and photocatalytic stability experiments also were performed. The detailed methods are described in ESI.

## 3. Results and discussion

### 3.1. Synthesis and characterization

MoS<sub>2</sub>/UiO-66-NH<sub>2</sub> heterojunctions were obtained on CFs by a hydrothermal-solvothermal two-step method, and then these fiber bundles were used to weave the fabrics (Fig. 1a). The color of original CFs is black and CF shows a diameter of 7.2 ± 0.5 μm (Fig. S1). After the first-step growth of MoS<sub>2</sub> on CFs, the color of the fiber sample turns darker (Fig. 1b). Scanning electronic microscopy (SEM) image (Fig. 1c) reveals that an obvious coating was obtained on each fiber surface. In addition, the average diameter of single fiber increases to 9.3 ± 0.5 μm (Fig. 1d). High-resolution (HR) SEM image (Fig. 1e) shows that this coating consists of thin nanosheets (thickness: ~5 nm, diameter: 200–400 nm), which should be MoS<sub>2</sub>. Besides, HR-SEM image of fractured surface (Fig. 1f) exhibits orderly nanosheet arrays arranged on the surface of CFs, confirming the successful growth of MoS<sub>2</sub> nanosheet arrays on the surface of CFs. MoS<sub>2</sub> can be firmly grew on CFs, due to the formation of Mo-O coordination bonding between Mo atoms from MoS<sub>2</sub> and -OH from the oxidized CF surface [29]. After the second-step growth of UiO-66-NH<sub>2</sub>, the color of the fibers is still black (Fig. 1g). There is no distinct change in the morphology (Fig. 1h) and the diameter of the fibers (Fig. 1i). HR-SEM image (Fig. 1j and k) shows the presence of many small nanoparticles (diameter: 20–40 nm) on the surface of MoS<sub>2</sub> nanosheets, suggesting the well decoration of UiO-66-NH<sub>2</sub> nanoparticles. It should be noted that there are close electrostatic interactions among Zr/O atoms from UiO-66-NH<sub>2</sub> and S/Mo atoms from MoS<sub>2</sub> [30], resulting in their well connection.

Subsequently, the composition of CFs/MoS<sub>2</sub>/UiO-66-NH<sub>2</sub> was measured by energy dispersive spectrometer (EDS). EDS pattern of CFs/MoS<sub>2</sub>/UiO-66-NH<sub>2</sub> (Fig. S2a) suggests the co-existence of C, Zr, Mo and S elements. C element should come from CF, Mo and S elements originate from MoS<sub>2</sub>, and Zr element exists in UiO-66-NH<sub>2</sub>. The elemental mapping results (Fig. S2b–f) indicate the uniformly distribution of these

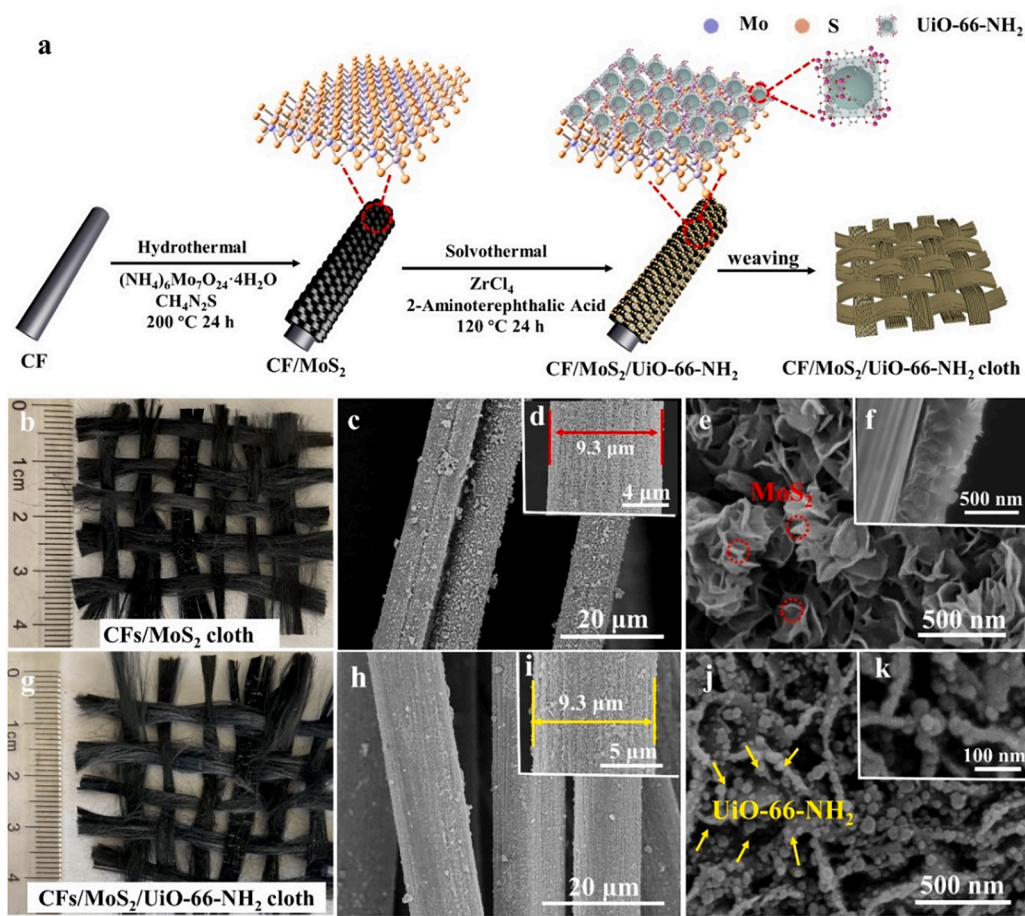


**Fig. 1.** (a) Synthesis scheme of CFs/MoS<sub>2</sub>/UiO-66-NH<sub>2</sub> bundles/cloth. Photo (b) and SEM images (c–f) of CFs/MoS<sub>2</sub> cloth. Photo (g) and SEM images (h–k) of CFs/MoS<sub>2</sub>/UiO-66-NH<sub>2</sub> cloth.

elements. To further analyze the structure, MoS<sub>2</sub>/UiO-66-NH<sub>2</sub> powder was peeled from CFs/MoS<sub>2</sub>/UiO-66-NH<sub>2</sub> and transmission electron microscopy (TEM) was applied to explore the microstructure. The typical TEM image (Fig. 2a) reveals that the powder is composed of thin nanosheets, which are decorated with thousands of nanoparticles. The

multitudinous nanosheets are stacked and intertwined together because of their ultrathin features. High-resolution TEM image (Fig. 2b) of the nanosheets displays a clear layer-shaped structure with a spacing of ~0.62 nm, which should be MoS<sub>2</sub> [31]. In addition, there are plenty of nanoparticles (diameter: 20–40 nm) attached to the nanosheets

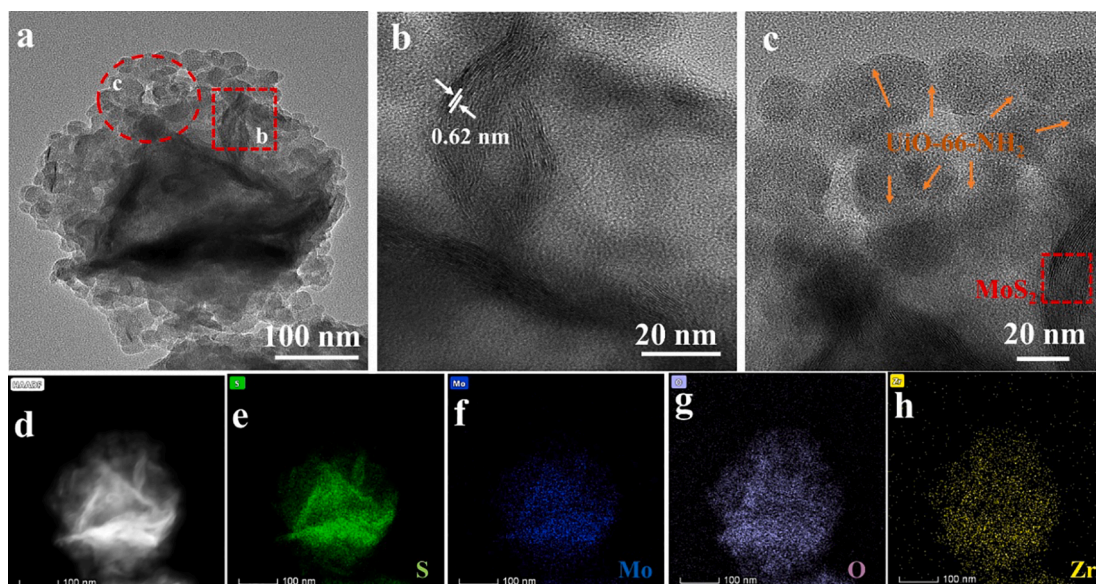


**Fig. 2.** TEM (a–c), HADDF-STEM (d) images and elemental mappings (e–h) of MoS<sub>2</sub>/UiO-66-NH<sub>2</sub> cloth.

(Fig. 2c), which should be UiO-66-NH<sub>2</sub> [32]. HADDF-STEM image (Fig. 2d) reveals the presence of multitudinous stacked nanosheets whose surface is decorated with some nanoparticles. Elemental mappings (Fig. 2e and f) confirm that elemental S and Mo are homogeneously distributed among stacked nanosheets, indicating that this nanosheet should be MoS<sub>2</sub>. In addition, elemental Zr and O are distributed among these nanoparticles (Fig. 2g and h), suggesting that nanoparticles should be UiO-66-NH<sub>2</sub>. Besides, the atomic ratio of O, Zr, Mo and S is equal to 12.01: 2.31: 16.38: 4.59, indicating that the molar ratio of MoS<sub>2</sub> to UiO-66-NH<sub>2</sub> is close to 2:1 (Table S1). Thus, the above results confirm the well formation of MoS<sub>2</sub>/UiO-66-NH<sub>2</sub> heterojunctions.

X-ray photoelectron spectroscopy (XPS) was applied to analyze the surface chemical composition and elemental valence states of three samples (MoS<sub>2</sub> powder, UiO-66-NH<sub>2</sub> powder and CFs/MoS<sub>2</sub>/UiO-66-NH<sub>2</sub>). Full survey spectra (Fig. 3a) reveal that MoS<sub>2</sub> powder is composed of Mo and S elements, while UiO-66-NH<sub>2</sub> powder consists of O and Zr elements. All these signals of these elements can be observed in CFs/MoS<sub>2</sub>/UiO-66-NH<sub>2</sub>. Mo 3d XPS spectrum in pure MoS<sub>2</sub> powder (Fig. 3b) shows two obvious peaks at 229.1 and 232.3 eV, which associated with the Mo 3d<sub>3/2</sub> and Mo 3d<sub>5/2</sub> [21]. Compared with MoS<sub>2</sub> powder, the Mo 3d<sub>3/2</sub> and Mo 3d<sub>5/2</sub> peak of CFs/MoS<sub>2</sub>/UiO-66-NH<sub>2</sub> appear at 229.3 and 232.5 eV, with a positive shift (~0.2 eV). It is worth noted that a weak S 2s peak appears at 226.6 eV of CFs/MoS<sub>2</sub>/UiO-66-NH<sub>2</sub>, which indicates the presence of S<sup>2-</sup> [33]. In the Zr 3d spectrum (Fig. 3c), pure UiO-66-NH<sub>2</sub> powder displays two obvious peaks at around 183 and 185.4 eV, which are related to the Zr 3d<sub>5/2</sub> and Zr 3d<sub>3/2</sub> [32]. Interestingly, Zr 3d<sub>5/2</sub> and Zr 3d<sub>3/2</sub> peaks of CFs/MoS<sub>2</sub>/UiO-66-NH<sub>2</sub> curve appear at 183.3 and 185.5 eV, with a positive shift (0.1 ~ 0.3 eV) compared with pure UiO-66-NH<sub>2</sub> powder. The changes in binding energies for Mo 3d and Zr 3d indicate the robust chemical bond between UiO-66-NH<sub>2</sub> and MoS<sub>2</sub> [34].

X-ray diffraction (XRD) spectrometry was applied to investigate the phase of samples. (Fig. 3d). XRD pattern of pure CFs shows a broad diffraction peak at ~25.96°, which can be ascribed to the (002) plane of the graphite structure. It should be noted that this peak can be found in

the XRD patterns of CFs/MoS<sub>2</sub> and CFs/MoS<sub>2</sub>/UiO-66-NH<sub>2</sub>. CFs/MoS<sub>2</sub> shows three new obvious diffraction peaks at 14.21°, 32.63° and 58.40°, corresponding to hexagonal phase MoS<sub>2</sub> (JCPDS No. 37-1492). UiO-66-NH<sub>2</sub> powder displays obvious five peaks at 7.68°, 8.82°, 25.24°, 43.50°, 56.70°, which is consistent with previous report [35]. Obviously, CFs/MoS<sub>2</sub>/UiO-66-NH<sub>2</sub> exhibits those three kinds of peaks, suggesting the good formation of hexagonal MoS<sub>2</sub> and UiO-66-NH<sub>2</sub> on CFs.

To explore the changes of specific surface area and total pore volume, N<sub>2</sub> adsorption-desorption isotherms of as-prepared samples were further conducted by Brunauer-Emmett-Teller (BET) method. These powders are peeled from fibers to avoid the negative effects of CF substrate on the surface area and pore size tests. MoS<sub>2</sub> powder shows a mesoporous structure with typical IV isotherm (Fig. 3e) with low surface area (20.6 m<sup>2</sup>/g), total pore volume (0.17 cm<sup>3</sup>/g) and large average pore diameter (~29.9 nm). It should be noted that the as-prepared MoS<sub>2</sub> shows a relatively large specific surface area compared with that in the related reports (Table S2). UiO-66-NH<sub>2</sub> exhibits an obvious microporous structure, and the curve is typical type I isotherm with a H3 hysteresis loop. The hysteresis loop appears for UiO-66-NH<sub>2</sub> at relative high pressure (P/P<sub>0</sub> > 0.8), which suggests the accumulation of pores [25]. Besides, UiO-66-NH<sub>2</sub> exhibits a high surface area (889.8 m<sup>2</sup>/g), total pore volume (0.91 cm<sup>3</sup>/g) and smallest average pore diameter (5.2 nm). The as-prepared UiO-66-NH<sub>2</sub> displays the largest specific surface area compared with that in the related publications (Table S2). After decorating UiO-66-NH<sub>2</sub> on MoS<sub>2</sub>, MoS<sub>2</sub>/UiO-66-NH<sub>2</sub> displays a hybrid type I/IV isotherm, revealing the existence of micropores and mesopores. Importantly, MoS<sub>2</sub>/UiO-66-NH<sub>2</sub> displays an enlarged surface area (245.9 m<sup>2</sup>/g) and total pore volume (0.52 cm<sup>3</sup>/g) compared with MoS<sub>2</sub>, suggesting that UiO-66-NH<sub>2</sub> nanoparticles greatly expand the specific surface area of MoS<sub>2</sub> powder. Usually, high surface area and total pore volume leads to efficient adsorption and photocatalytic activity [36]. Besides, the pore size distribution (Fig. 3f) of samples are very narrow, implying good homogeneity of the pores. The existing micropores and mesopores in these samples provide transport paths for pollutants in photocatalytic reactions. Thus, these unique pore characteristics and

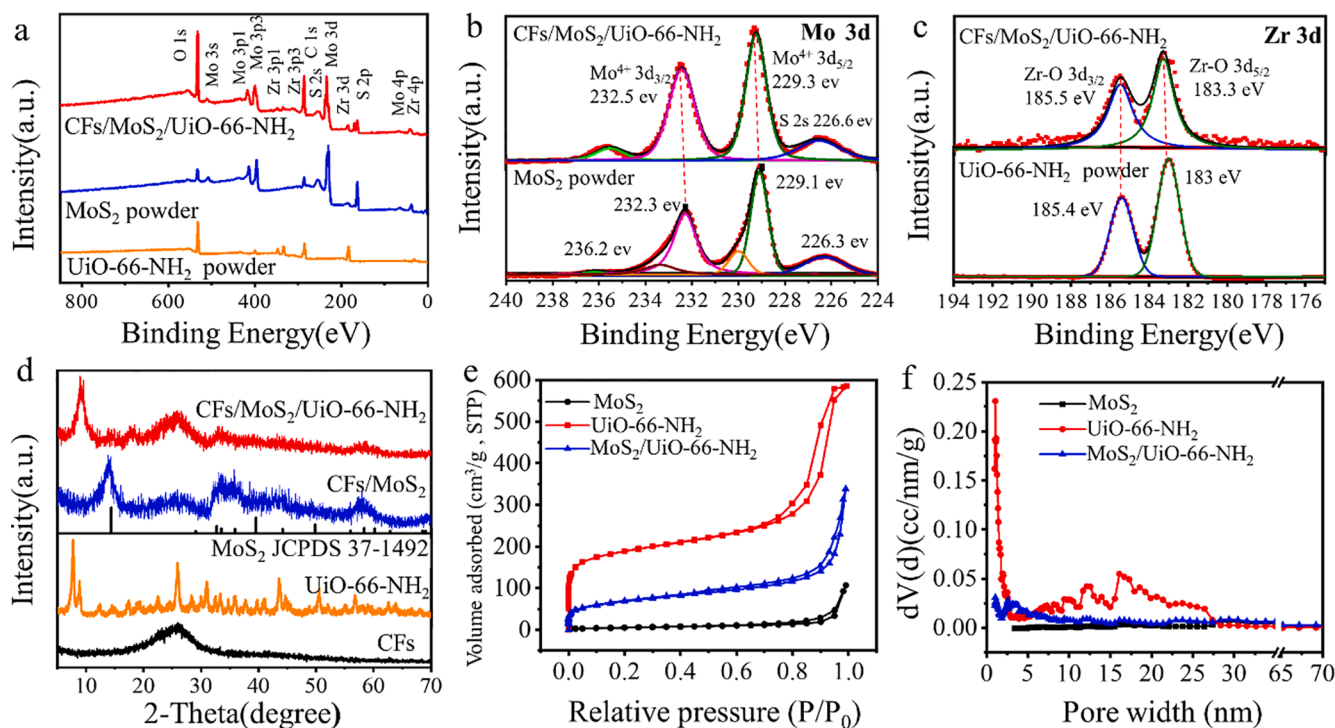


Fig. 3. (a) XPS survey spectra for MoS<sub>2</sub> powder, UiO-66-NH<sub>2</sub> powder and CFs/MoS<sub>2</sub>/UiO-66-NH<sub>2</sub>; High-resolution XPS spectra of Mo 3d (b) and Zr 3d (c). (d) XRD patterns of different samples; N<sub>2</sub> adsorption-desorption isotherms (e) and Pore size distribution (f) of MoS<sub>2</sub>, UiO-66-NH<sub>2</sub> and CFs/MoS<sub>2</sub>/UiO-66-NH<sub>2</sub>.

large specific surface area endow  $\text{MoS}_2/\text{UiO-66-NH}_2$  with more active sites, which benefit to the improvement of the catalytic activity.

### 3.2. Optical and photoelectrochemical measurements

To investigate the photoabsorption, different samples were analyzed by UV-Vis-NIR diffuse reflectance spectra (Fig. 4a). Pure CFs shows a broad photoabsorption in 200–800 nm, owing to the efficient scattering/absorption of light among CFs' texture and pore structure [37]. Similarly, CFs/ $\text{MoS}_2$  shows strong and broad photoabsorption, which is consistent with that of pure  $\text{MoS}_2$  (Fig. S3a), resulting from the co-effect of the band-gap absorption, scattering and plasmon resonance, similar to the previous report [38].  $\text{UiO-66-NH}_2$  exhibits an absorption edge at 464 nm. Comparing to  $\text{UiO-66-NH}_2$ , the absorption of CFs/ $\text{MoS}_2/\text{UiO-66-NH}_2$  displays a slight redshift (edge: 470 nm), which demonstrates that the construction of  $\text{MoS}_2/\text{UiO-66-NH}_2$  has no adverse influence on the optical property. Moreover, the Kubelka-Munk transformed reflectance spectra of  $\text{MoS}_2$  (Fig. S3b) and  $\text{UiO-66-NH}_2$  (Fig. 4b) powders were performed based on the equation  $(\alpha h\nu)^n = A(h\nu - E_g)$  to estimate their band-gap energy ( $E_g$ ) [6]. The bandgap energies ( $E_g$ ) of  $\text{MoS}_2$  and  $\text{UiO-66-NH}_2$  are estimated to be 1.87 and 2.67 eV, respectively.

Furthermore, to explore the conduction band (CB) and valence band (VB) potentials ( $E_{\text{CB}}$  and  $E_{\text{VB}}$ ), the Mott-Schottky (MS) plots were employed. As shown in Fig. 4c and d, the MS plot slopes of  $\text{MoS}_2$  and  $\text{UiO-66-NH}_2$  are positive, suggesting that they are n-type semiconductors [20]. The x-intercepts of the two lines are around  $-0.7$  and  $-0.85$  eV vs.  $\text{Ag}/\text{AgCl}$ , which is calculated as  $U_{\text{fb}}$ . Since  $U_{\text{fb}}$  is very close to the

conduction band (CB) potential ( $E_{\text{CB}}$ ) for n-type semiconductors [39,40]. Thus, the  $E_{\text{CB}}$  of  $\text{MoS}_2$  and  $\text{UiO-66-NH}_2$  are estimated to be  $-0.5$  and  $-0.65$  eV vs NHE. Furthermore, the valence band (VB) potential ( $E_{\text{VB}}$ ) of  $\text{MoS}_2$  and  $\text{UiO-66-NH}_2$  can be calculated by the following equation:  $E_{\text{VB}} = E_{\text{CB}} + E_g$ . The  $E_{\text{VB}}$  of  $\text{MoS}_2$  and  $\text{UiO-66-NH}_2$  are 1.37 and 2.02 eV vs NHE, respectively.

To explore the charge separation efficiency during the photocatalytic process, ITO glass with samples was constructed as a working electrode. I-t study (Fig. 5a) was tested by four ON/OFF cycles at 0.5 V vs. SCE. Under visible light illumination, the current density of CFs/ $\text{MoS}_2/\text{UiO-66-NH}_2$  cloth rises immediately and maintains at a stable value of  $3.8 \mu\text{A}/\text{cm}^2$ , which is higher than that of CFs/ $\text{MoS}_2$  ( $\sim 2.4 \mu\text{A}/\text{cm}^2$ ) and CFs/ $\text{UiO-66-NH}_2$  ( $\sim 0.9 \mu\text{A}/\text{cm}^2$ ) cloths. When the light is off, the currents of these cloths drop and return to the initial value. This phenomenon is repeatable in four cycles, which indicates the high stability of as-prepared samples. Furthermore, the electrochemical impedance spectrum (EIS) (Fig. 5b) was applied to research the electron transfer resistance. A smaller arc radius indicates a higher charge transfer speed [41]. The Nyquist impedance spectra show that arc radius of CFs/ $\text{MoS}_2$  and CFs/ $\text{UiO-66-NH}_2$  cloths are significantly smaller than CFs. Interestingly, CFs/ $\text{MoS}_2/\text{UiO-66-NH}_2$  displays the smallest arc size, suggesting the lowest electrical impedance. Therefore, CFs/ $\text{MoS}_2/\text{UiO-66-NH}_2$  cloth possesses the highest photocurrent and lowest recombination rate of photo-excited charge carriers.

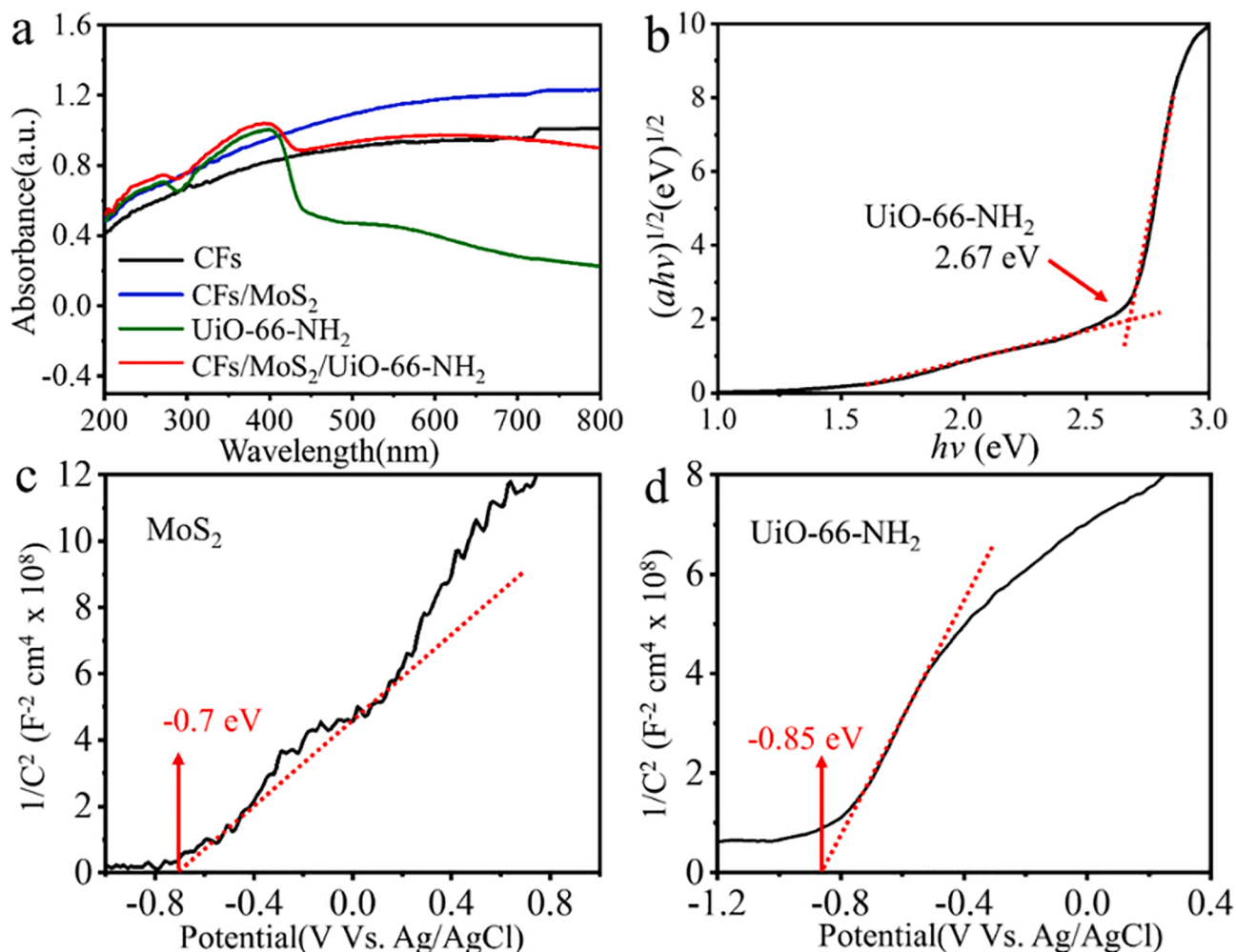


Fig. 4. (a) UV-Vis-NIR spectra of the as-prepared cloths; (b) calculated band gaps of  $\text{UiO-66-NH}_2$ . Mott-Schottky plots of  $\text{MoS}_2$  (c) and  $\text{UiO-66-NH}_2$  (d).

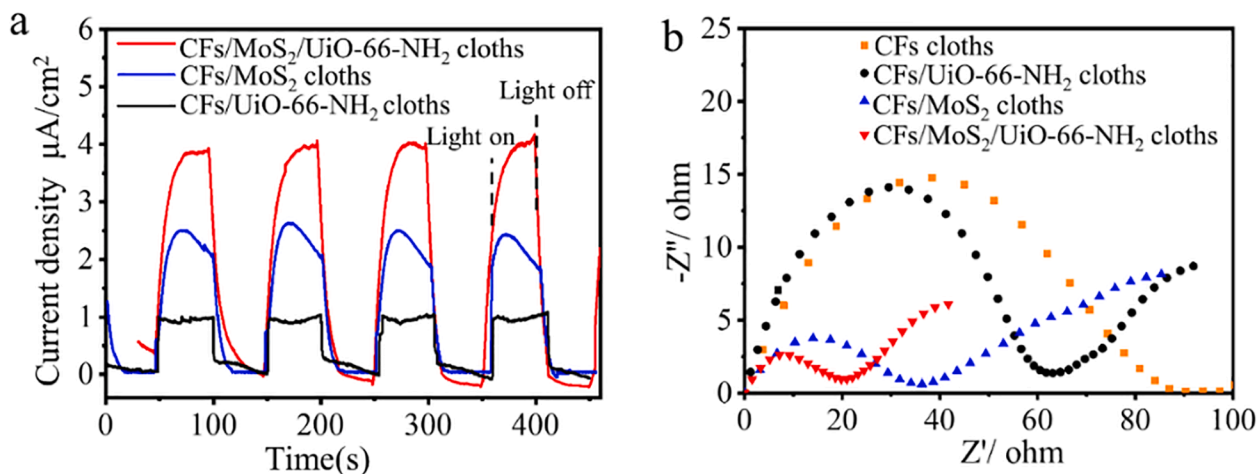


Fig. 5. Photocurrent responses (a) and EIS (b) of as-prepared cloths.

### 3.3. Removal efficiency

The adsorption and photocatalytic performances of as-prepared

cloths were investigated via the removal of LVFX (100 mL, 20 mg/L) and Cr(VI) (100 mL, 50 mg/L) (Fig. 6a). In the dark, CFs cloth can only adsorb 1.2% LVFX and 1.7% Cr(VI), resulting from its low specific

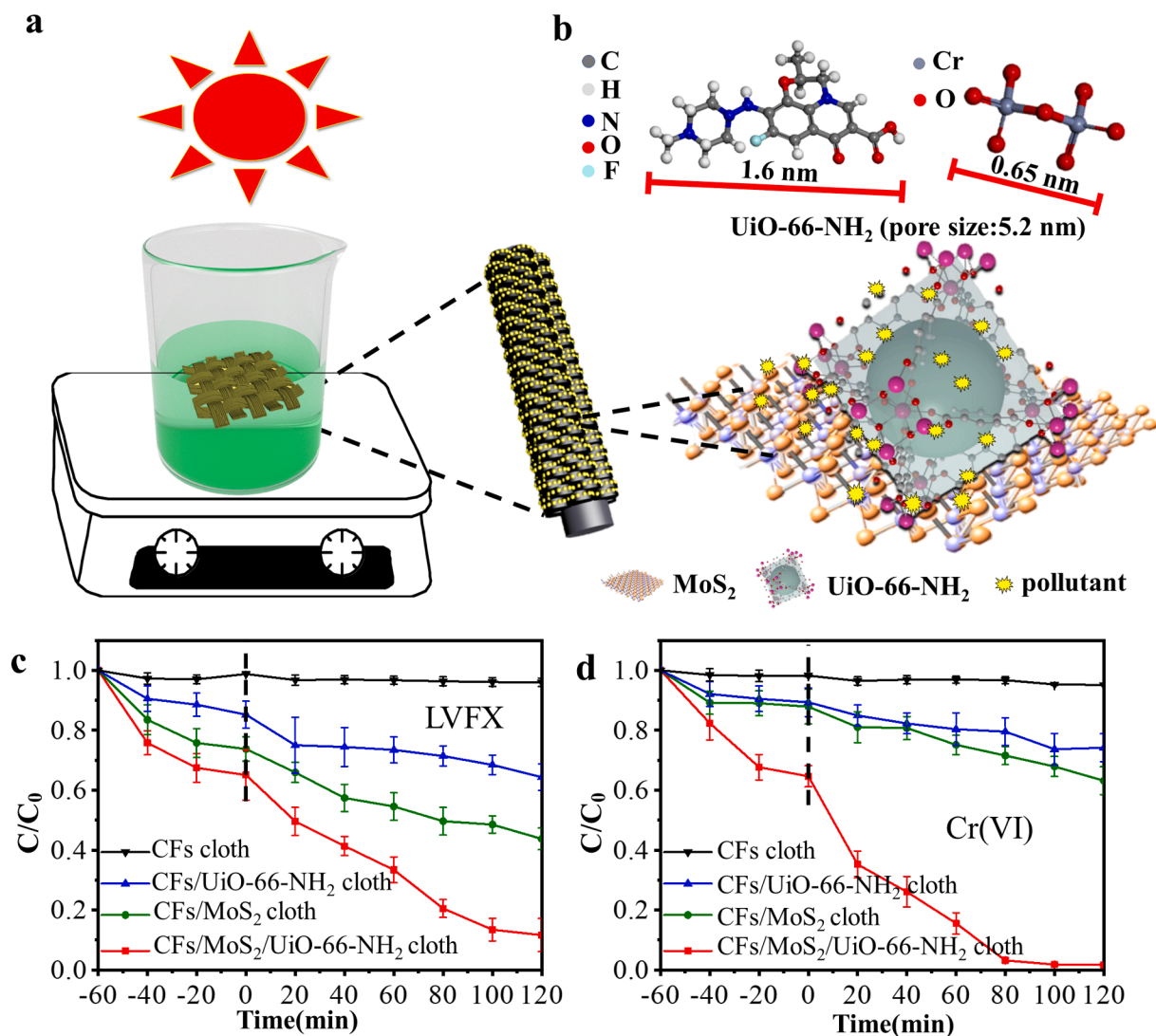


Fig. 6. Schemes of the photocatalytic reaction system (a) and the adsorption process (b) by CFs/MoS<sub>2</sub>/UiO-66-NH<sub>2</sub> bundle; The adsorption and degradation efficiency of LVFX (20 mg/L) (c) and Cr(VI) (50 mg/L) (d) with different catalysts under visible light irradiation.

surface area (about  $0.33 \text{ m}^2/\text{g}$ ). CFs/MoS<sub>2</sub> cloth displays enhanced adsorption capacity towards LVFX (26.2%) and Cr(VI) (12%), since the layer-shaped structure of MoS<sub>2</sub> nanosheets increases the specific absorption sites. Besides, CFs/UiO-66-NH<sub>2</sub> can efficiently adsorb 14.8% LVFX and 10.7% Cr(VI). After decorating UiO-66-NH<sub>2</sub> on CFs/MoS<sub>2</sub>, the obtained CFs/MoS<sub>2</sub>/UiO-66-NH<sub>2</sub> cloth displays 1.3–2.9 times adsorption capacity for LVFX (34.9%) and Cr(VI) (35.3%) compared with CFs/MoS<sub>2</sub> cloth (26.2% LVFX and 12.0% Cr(VI)). Adsorption efficiency of CFs/UiO-66-NH<sub>2</sub> cloth is worse than that of CFs/MoS<sub>2</sub>/UiO-66-NH<sub>2</sub> cloth, probably due to the low load capacity of UiO-66-NH<sub>2</sub> on CFs in CFs/UiO-66-NH<sub>2</sub> sample (Fig. S4). While for CFs/MoS<sub>2</sub>/UiO-66-NH<sub>2</sub>, MoS<sub>2</sub> nanosheets promote the growth of UiO-66-NH<sub>2</sub> nanoparticles. Based on the experimental results, the adsorption ratio of CFs:UiO-66-NH<sub>2</sub>:MoS<sub>2</sub> in CFs/MoS<sub>2</sub>/UiO-66-NH<sub>2</sub> cloth can be calculated to be 1:15:26 for LVFX or 1:5:6 for Cr(VI). CFs/MoS<sub>2</sub>/UiO-66-NH<sub>2</sub> cloth can absorb more Cr(VI) than LVFX attribute to the fact that Cr(VI) is charged and easier to be adsorbed on the catalyst surface and inside. Obviously, the enhanced adsorption ability of CFs/MoS<sub>2</sub>/UiO-66-NH<sub>2</sub> cloth should be resulted from the decoration of UiO-66-NH<sub>2</sub> with large surface area ( $889.8 \text{ m}^2/\text{g}$ ) and total pore volume ( $0.91 \text{ cm}^3/\text{g}$ ). The large surface area provides a lot of active site for pollutants, which contribute to the adsorption of pollutants by CFs/MoS<sub>2</sub>/UiO-66-NH<sub>2</sub> cloth. Besides, the pore size (5.2 nm) of UiO-66-NH<sub>2</sub> is larger than that of LVFX (1.6 nm) or Cr(VI) (0.65 nm) (Fig. 6b), which were calculated by Materials Studio. The large pore size of UiO-66-NH<sub>2</sub> facilitates the entrance of LVFX or Cr(VI) molecule, contributing to the well distribution/loading on their surface and the interior. Besides, CFs/MoS<sub>2</sub>/UiO-66-NH<sub>2</sub> cloth shows better adsorption capacity compared with other materials in the literature, such as Ag/AgCl@ZIF-8/CN (20% LVFX) [42], ZnFe<sub>2</sub>O<sub>4</sub>/NCDs/Ag<sub>2</sub>CO<sub>3</sub> (13% LVFX) [43], Pd@UiO-66(NH<sub>2</sub>) (10% Cr(VI)) [25] or UiO-66(NH<sub>2</sub>) (4% Cr(VI)) [44].

When the xenon lamp is turned on, no LVFX can be degraded by CFs

cloth, proving that CF has no photo-degradation ability towards LVFX. CFs/MoS<sub>2</sub> can degrade 56.3% LVFX molecules in 120 min, which is better than CFs/UiO-66-NH<sub>2</sub> (35.6%). Importantly, CFs/MoS<sub>2</sub>/UiO-66-NH<sub>2</sub> cloth can remove 88.4% LVFX molecular in 120 min, which is 1.6 times compared with that by CFs/MoS<sub>2</sub> cloth (56.3%) (Fig. 6c). Besides, Cr(VI) was selected to test the photo-reduction effect of CFs/MoS<sub>2</sub>/UiO-66-NH<sub>2</sub> cloth. CFs/MoS<sub>2</sub>/UiO-66-NH<sub>2</sub> cloth absorbs visible light and quickly reduce the toxic Cr(VI) to low-toxic Cr(III). Only 36.9% and 25.8% Cr(VI) can be reduced to Cr(III) by CFs/MoS<sub>2</sub> or CFs/UiO-66-NH<sub>2</sub> cloths after 120 min. Importantly, CFs/MoS<sub>2</sub>/UiO-66-NH<sub>2</sub> cloth can remove 98.4% Cr(VI) after 120 min, which is 2.7 times compared with that (36.9%) by CFs/MoS<sub>2</sub> (Fig. 6d). These experimental facts strongly suggest that CFs/MoS<sub>2</sub>/UiO-66-NH<sub>2</sub> is capable of removing LVFX and reducing Cr(VI) from wastewater under the visible-light irradiation. Furthermore, the photocatalytic activity for degradation of LVFX and Cr(VI) by prepared CFs/MoS<sub>2</sub>/UiO-66-NH<sub>2</sub> cloth under visible light irradiation were compared with other previous reported photocatalysts. For example, Zhou et al. studied that Ag/AgCl@ZIF-8/CN composite can remove 87.3% LVFX within 60 min [42]. Liang and his colleagues designed layered 2D/2D Bi@Bi<sub>5</sub>O<sub>7</sub>I/rGO heterojunction composite. The novel composite could photocatalytically remove 87.7% LVFX [45] and Liang et al. reported that MIL-68(In)-NH<sub>2</sub> could reduce 97% Cr(VI) in 180 min under visible light irradiation [46]. Notably, the as-synthesized CFs/MoS<sub>2</sub>/UiO-66-NH<sub>2</sub> cloth not only exhibits higher photocatalytic activity towards LVFX and Cr(VI) compared with related publications, but also owns a simple recovery process.

Furthermore, the effects of pH values were studied by using CFs/MoS<sub>2</sub>/UiO-66-NH<sub>2</sub> cloth. In the photocatalytic experiments, four different pH values (range: 2.15–11.13) were adjusted in LVFX (20 mg/L, 100 mL) solution (Fig. 7a). With pH value increases from 2.15 to 5.18, the corresponding LVFX removal efficiency goes up from 56.8% to 88.4%. However, when further increase pH from 5.18 to 11.13, the

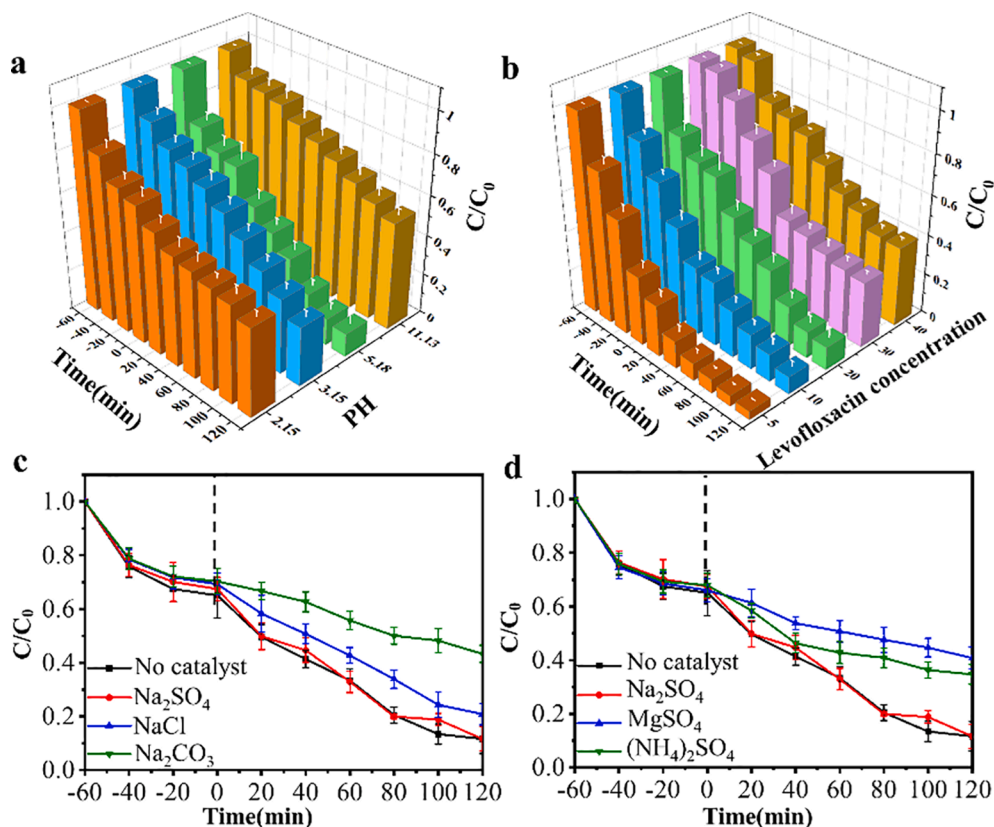


**Fig. 7.** Effect of pH (a) and LVFX concentration (b) on degradation efficiency by CFs/MoS<sub>2</sub>/UiO-66-NH<sub>2</sub> cloth; Influence of Na<sub>2</sub>SO<sub>4</sub>, NaCl, Na<sub>2</sub>CO<sub>3</sub> (c) and Na<sub>2</sub>SO<sub>4</sub>, MgSO<sub>4</sub>, (NH<sub>4</sub>)<sub>2</sub>SO<sub>4</sub> (d) on photocatalytic activity over CFs/MoS<sub>2</sub>/UiO-66-NH<sub>2</sub> cloth.

degradation efficiency goes down to 46.0%. This phenomenon could be interpreted as follows: LVFX antibiotics have two  $pK_a$  values, where  $pK_{a1}$  and  $pK_{a2}$  are 5.33 and 8.07, respectively [47]. Thus, when the pH is 2.15 or 3.15, LVFX becomes a cationic molecule, and the surface charge of CFs/MoS<sub>2</sub>/UiO-66-NH<sub>2</sub> cloth is also positive, resulting in electrostatic repulsion force and reduces the adsorption and photodegradation capability. Similarly, when pH is 11.13, there is an inhibition in the adsorption attribute to the repulsive force between the anionic LVFX and the negative surface charge of the CFs/MoS<sub>2</sub>/UiO-66-NH<sub>2</sub> cloth. Besides, alkaline conditions will inhibit the production of  $\cdot O_2^-$ , resulting in a decrease in the degradation efficiency [48]. When the pH is 5.18, the surface charge of the CFs/MoS<sub>2</sub>/UiO-66-NH<sub>2</sub> cloth and ionization conditions of LVFX solution could be converted between positive and neutral state, the surface holes generated constantly. Thus, CFs/MoS<sub>2</sub>/UiO-66-NH<sub>2</sub> cloth shows superior efficiency under weak acid conditions.

The effects of the initial LVFX concentration (5–40 mg/L) were evaluated by using CFs/MoS<sub>2</sub>/UiO-66-NH<sub>2</sub> (weight: 0.15 g) under visible light illumination (Fig. 7b). With the increase of LVFX concentration from 5 to 40 mg/L, the degradation efficiency by CFs/MoS<sub>2</sub>/UiO-66-NH<sub>2</sub> cloth decreases from 95.8% to 60.0%. The decreased efficiency should be result from the fact that high concentration of LVFX cover some active sites on cloth, obstruct the penetration of light as well as impede the photogenerated electrons to reach the surface of the LVFX drug. Besides, there are many inorganic ions in practical wastewater that can affect the removal of target pollutants. In this study, Na<sub>2</sub>SO<sub>4</sub>, NaCl, Na<sub>2</sub>CO<sub>3</sub>, MgSO<sub>4</sub> and (NH<sub>4</sub>)<sub>2</sub>SO<sub>4</sub> were added as influencing ions. With Na<sub>2</sub>SO<sub>4</sub> as an influencing ion, the degradation efficiency of CFs/MoS<sub>2</sub>/

UiO-66-NH<sub>2</sub> cloth maintains at 88.4%, indicating that the effects of Na<sub>2</sub>SO<sub>4</sub> on photocatalytic activity can be neglected. When NaCl or Na<sub>2</sub>CO<sub>3</sub> is added into the LVFX solution, the degradation efficiency of the cloth distinctly decreases from 88.4% to 79.2% (NaCl) or 56.7% (Na<sub>2</sub>CO<sub>3</sub>) (Fig. 7c). The inhibition of Cl<sup>-</sup> on degradation efficiency should be resulted from the inevitable competitive adsorption between Cl<sup>-</sup> and LVFX. While CO<sub>3</sub><sup>2-</sup> is known to serve as a radical scavenger, which can consume  $\cdot OH$  radicals generated in the photocatalytic reaction [45]. (NH<sub>4</sub>)<sub>2</sub>SO<sub>4</sub> and MgSO<sub>4</sub> show significant inhibition for the degradation of LVFX (Fig. 7d), with the corresponding degradation efficiency drop from 88.4% to 65.3% ((NH<sub>4</sub>)<sub>2</sub>SO<sub>4</sub>) or 59.2% (MgSO<sub>4</sub>). The decrease in photocatalytic performance can be explained by the competition of NH<sub>4</sub><sup>+</sup> and Mg<sup>2+</sup> over the active sites with LVFX, which may increase the difficulty in degrading LVFX [49]. The above results demonstrate that the existence of Cl<sup>-</sup>, CO<sub>3</sub><sup>2-</sup>, Mg<sup>2+</sup> and NH<sub>4</sub><sup>+</sup> ions inhibit the degradation efficiency of LVFX by CFs/MoS<sub>2</sub>/UiO-66-NH<sub>2</sub> cloth.

To explore the main reactive species, different capture agents were put into the LVFX solution. Apparently, with ammonium oxalate (AO) or isopropyl alcohol (IPA) as scavengers to capture h<sup>+</sup> or  $\cdot OH$ , there is no apparent change in the photodegradation efficiency (Fig. 8a). The corresponding rate constant is 0.02591 min<sup>-1</sup> (AO) or 0.01588 min<sup>-1</sup> (IPA) (Fig. S5a). However, when silver nitrate (AgNO<sub>3</sub>) or benzoquinone (BQ) is added as scavengers to capture e<sup>-</sup> or  $\cdot O_2^-$ , the degradation efficiency of LVFX distinctly decrease from 88.4% to 29.6% or 9.4% with the corresponding rate of 0.00306 min<sup>-1</sup> (AgNO<sub>3</sub>) or 0.00153 min<sup>-1</sup> (BQ), respectively. The above results indicate that  $\cdot O_2^-$  and e<sup>-</sup> are the main reactive species during the photodegradation of LVFX by CFs/MoS<sub>2</sub>/

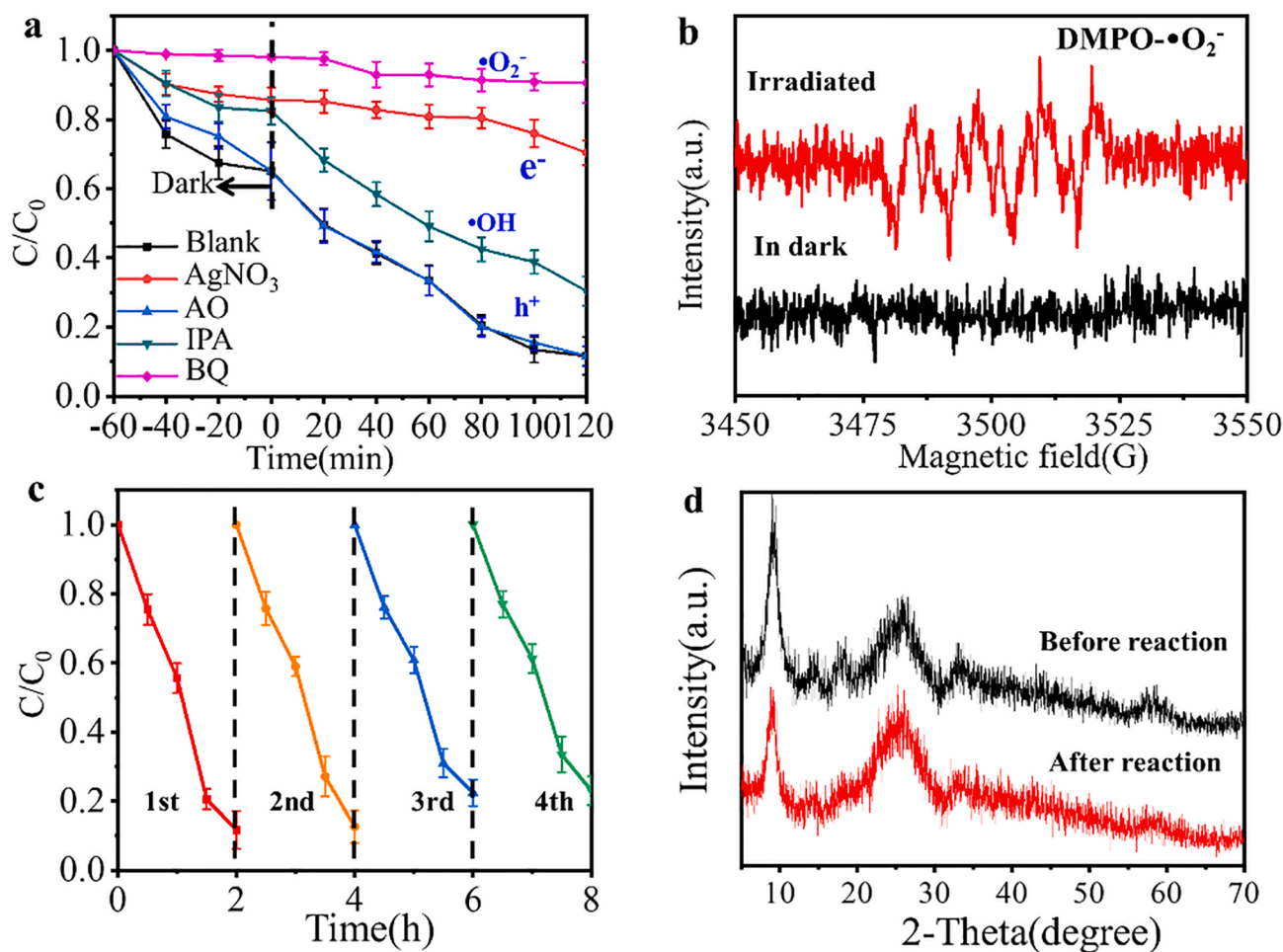


Fig. 8. (a) LVFX removal efficiency and reaction kinetics with various scavengers. (b) ESR spectra for DMPO·O<sub>2</sub><sup>-</sup>. (c) Multicycle run experiment in removing LVFX and (d) XRD pattern of the cloth before/after the photocatalytic reaction.

UiO-66-NH<sub>2</sub> cloth. Electron spin resonance (ESR) tests were applied to test the signal of  $\cdot\text{O}_2^-$  and  $\cdot\text{OH}$ . After illuminated by visible light for 10 min, ESR spectrum of DMPO- $\cdot\text{O}_2^-$  (Fig. 8b) exhibits obvious characteristic peaks, indicating the existence of  $\cdot\text{O}_2^-$ . However, ESR spectrum of DMPO- $\cdot\text{OH}$  (Fig. S5b) exhibits several weak peaks, implying that few  $\cdot\text{OH}$  radicals were produced. Therefore, the ESR experiments further confirm that  $\cdot\text{O}_2^-$  is the main reactive specie in the photo-degradation process of LVFX by CFs/MoS<sub>2</sub>/UiO-66-NH<sub>2</sub> cloth.

The recycling ability and stability of CFs/MoS<sub>2</sub>/UiO-66-NH<sub>2</sub> cloth was studied by 4-cycle tests. Before each cycle, CFs/MoS<sub>2</sub>/UiO-66-NH<sub>2</sub> (area: 4 × 4 cm<sup>2</sup>, weight: 0.15 g) was taken out from the reaction system by tweezers, washed by deionized water several times and immersed into the deionized water overnight, then dried (60 °C, 6 h). CFs/MoS<sub>2</sub>/UiO-66-NH<sub>2</sub> cloth shows a slightly downward trend in LVFX removal efficiency from the first cycle (88.4%) to the fourth cycle (76.9%) (Fig. 8c), probably resulting from the surface area reduction (Table S3) and the fact that many pollutants were absorbed on the surface of cloth, leading incomplete LVFX desorption. Moreover, XRD pattern (Fig. 8d) and SEM images (Fig. S6) of used CFs/MoS<sub>2</sub>/UiO-66-NH<sub>2</sub> cloth are similar to those of the original sample. Besides, the cost of CFs/MoS<sub>2</sub>/UiO-66-NH<sub>2</sub> was estimated to be approximately \$ 0.8/g (Table S4-S6). CFs were used for 10 times at an average cost of \$ 0.08/g each time, indicating a low cost (the detailed calculations are presented in the ESI). To further confirm the stability of CFs/MoS<sub>2</sub>/UiO-66-NH<sub>2</sub> cloth, the leakage of Mo and Zr ions in the solution after each photocatalytic cycle was monitored by inductively coupled plasma optical emission spectrometer (ICP-OES) analysis (Fig. S7). The released Mo and Zr (% of original) are all less than 3% during 1–4 cycles (2–8 h), demonstrating the good chemical stability of CFs/MoS<sub>2</sub>/UiO-66-NH<sub>2</sub> cloth. Thus, CFs/MoS<sub>2</sub>/UiO-66-NH<sub>2</sub> cloth possesses good recyclability and stability for photodegrading the wastewater.

To investigate the degradation pathways of LVFX by CFs/MoS<sub>2</sub>/UiO-66-NH<sub>2</sub> cloth, liquid chromatography-tandem mass spectrometry (LC-MS) was carried out to observe intermediates products. According to the mass spectra (Fig. S8), we summarized the possible intermediates

products of LVFX degradation (Table S7) and photocatalytic degradation pathways (Fig. 9). Product 1 ( $m/z = 322$ ) and product 2 ( $m/z = 340$ ) are due to the loss of C<sub>3</sub>H<sub>4</sub> or HF molecules from the LVFX parent. The main degradation path is as follows: Product 3 ( $m/z = 318$ ), 4 ( $m/z = 235$ ) and 5 ( $m/z = 218$ ) ascribes to the decarboxylation, the removal of piperazinyl group and defluorination step. In addition, LVFX molecule can be oxidized to Product 6 ( $m/z = 307$ ). Product 7 ( $m/z = 263$ ), 4 ( $m/z = 235$ ) and 5 ( $m/z = 218$ ) appear due to the decarboxylation of Product 6 ( $m/z = 307$ ). Product 8 ( $m/z = 227$ ) are formed and can be assigned to a series of dehydration processes. Product 10 ( $m/z = 264$ ) is formed due to the removal of piperazinyl group of Product 9 ( $m/z = 292$ ). These byproducts might be further oxidized into small molecular products or mineralized inorganic compounds. These facts illustrate that CFs/MoS<sub>2</sub>/UiO-66-NH<sub>2</sub> cloth can effectively degrade LVFX under the visible-light irradiation.

### 3.4. Mechanisms

According to the above results, CFs/MoS<sub>2</sub>/UiO-66-NH<sub>2</sub> cloth exhibits the high removal efficiencies toward LVFX and Cr(VI). High removal efficiencies probably result from the following two advantages, as shown in the mechanism scheme (Fig. 10). One is the improvement of adsorption (1.3–2.9 times) after decorating UiO-66-NH<sub>2</sub>. CFs/MoS<sub>2</sub>/UiO-66-NH<sub>2</sub> cloth displays good adsorption and diffusion of pollutant molecules, resulting from its open channels, high specific surface area (245.9 m<sup>2</sup>/g) and total pore volume (0.52 cm<sup>3</sup>/g), as confirmed by Fig. 3e and f. The other one is the two-component synergistic photocatalytic capability. After decorating UiO-66-NH<sub>2</sub>, the obtained cloth retains the strong photoabsorption (Fig. 6) and shows the highest photocurrent and the lowest recombination rate (Fig. 5a and b). Under visible light, both MoS<sub>2</sub> and UiO-66-NH<sub>2</sub> component can be excited to produce photogenerated electrons. Since the  $E_{CB}$  of UiO-66-NH<sub>2</sub> is more negative than that of MoS<sub>2</sub>, the photogenerated electrons in CB of UiO-66-NH<sub>2</sub> would shift to the CB of MoS<sub>2</sub>. Subsequently, the electrons in MoS<sub>2</sub> can further flow to the conductive CF and reduce O<sub>2</sub> to generate

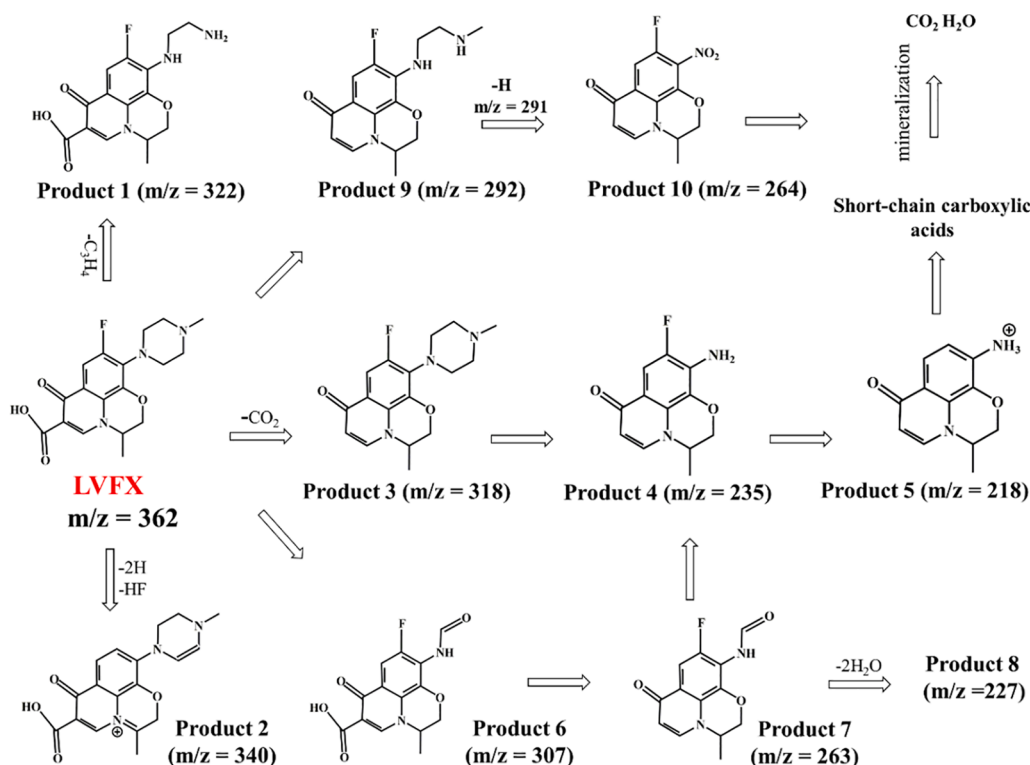


Fig. 9. Possible photo-degradation pathway of LVFX by CFs/MoS<sub>2</sub>/UiO-66-NH<sub>2</sub> cloth.

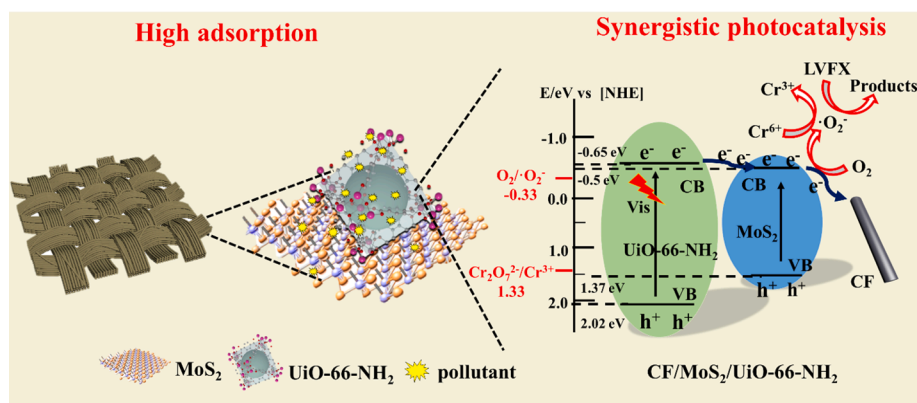


Fig. 10. Schematic illustration of adsorption and photocatalysis mechanism of CFs/MoS<sub>2</sub>/UiO-66-NH<sub>2</sub> cloth.

•O<sub>2</sub><sup>-</sup>, thus promote LVFX molecule degradation. All the above advantages together endow the CFs/MoS<sub>2</sub>/UiO-66-NH<sub>2</sub> cloth with superior adsorption and photocatalytic performance during removing pollutants (Fig. 6c and d).

#### 4. Conclusions

UiO-66-NH<sub>2</sub> nanoparticles have been used as a model of MOF to decorate MoS<sub>2</sub> nanosheets on CFs. UiO-66-NH<sub>2</sub> nanoparticles with the size of 20–40 nm greatly improve the surface area (20.6 m<sup>2</sup>/g MoS<sub>2</sub>, 245.9 m<sup>2</sup>/g MoS<sub>2</sub>/UiO-66-NH<sub>2</sub>) and total pore volume (0.17 cm<sup>3</sup>/g MoS<sub>2</sub>, 0.52 cm<sup>3</sup>/g MoS<sub>2</sub>/UiO-66-NH<sub>2</sub>). After the decoration of UiO-66-NH<sub>2</sub>, there are two obvious improvements. The first one is the improvement of adsorption capacity. In the dark, the weaved CFs/MoS<sub>2</sub>/UiO-66-NH<sub>2</sub> cloth exhibits remarkable enhanced adsorbing capacity by adsorbing more LVFX molecules (34.9%) and Cr(VI) (35.3%), which is 1.3–2.9 times than that by CFs/MoS<sub>2</sub> cloth (26.2% LVFX and 12.0% Cr(VI)) in 60 min. Another one is the improvement of photocatalytic performance. Under visible-light irradiation, the cloth shows excellent photocatalytic ability (88.4%/98.4%) of removing LVFX and Cr(VI), which is 1.6–2.7 times higher than that by CFs/MoS<sub>2</sub> cloth (56.3% LVFX and 36.9% Cr(VI)) within 120 min. Furthermore, efficient and low-cost CFs/MoS<sub>2</sub>/UiO-66-NH<sub>2</sub> cloth can be easily taken out and used, and there are no obvious changes in their crystalline phase/morphologies and shows slight negative influence on photocatalytic activity during four-cycle tests. Meanwhile, in the economical dimension, the efficient, low-cost and recyclable CFs/MoS<sub>2</sub>/UiO-66-NH<sub>2</sub> cloth can greatly save economic costs while retaining high efficiency. In the future work, more effort will be put on developing new methods to continuously grow MoS<sub>2</sub>/UiO-66-NH<sub>2</sub> junctions on ultralong CFs, and then these obtained CFs/MoS<sub>2</sub>/UiO-66-NH<sub>2</sub> fiber can be weaved to large-area three-dimensional fabrics as photocatalytic membrane to purify the flowing wastewater under visible light irradiation. Therefore, our work provides new ideas for constructing semiconductor/MOFs-based heterojunction on CF for photocatalytic degradation of contaminants in water.

#### CRedit authorship contribution statement

**Wei Cao:** Investigation, Methodology, Writing - original draft. **Yan Zhang:** Investigation, Methodology, Writing - original draft. **Zhun Shi:** Investigation. **Ting Liu:** Investigation. **Xinshan Song:** . **Lisha Zhang:** Funding acquisition, Project administration. **Po Keung Wong:** . **Zhi-gang Chen:** Project administration.

#### Declaration of Competing Interest

The authors declare that they have no known competing financial

interests or personal relationships that could have appeared to influence the work reported in this paper.

#### Acknowledgements

This work was financially supported by the National Natural Science Foundation of China (51972056, 51773036), National Key Research and Development Program of China (2019YFC0408604), Shanghai Shuguang Program (18SG29), Natural Science Foundation of Shanghai (18ZR1401700), Innovation Program of Shanghai Municipal Education Commission (2017-01-07-00-03-E00055), the Fundamental Research Funds for the Central Universities and Graduate Student Innovation Fund of Donghua University (CUSF-DH-D-2020070), and DHU Distinguished Young Professor Program.

#### Appendix A. Supplementary data

Supplementary data to this article can be found online at <https://doi.org/10.1016/j.cej.2020.128112>.

#### References

- [1] W. Wang, Q. Niu, G. Zeng, C. Zhang, D. Huang, B. Shao, C. Zhou, Y. Yang, Y. Liu, H. Guo, W. Xiong, L. Lei, S. Liu, H. Yi, S. Chen, X. Tang, 1D porous tubular g-C<sub>3</sub>N<sub>4</sub> capture black phosphorus quantum dots as 1D/0D metal-free photocatalysts for oxytetracycline hydrochloride degradation and hexavalent chromium reduction, *Appl. Catal. B: Environ.* 273 (2020), 119051, <https://doi.org/10.1016/j.apcatb.2020.119051>.
- [2] S. Wu, H. He, X. Li, C. Yang, G. Zeng, B. Wu, S. He, L. Lu, Insights into atrazine degradation by persulfate activation using composite of nanoscale zero-valent iron and graphene: performances and mechanisms, *Chem. Eng. J.* 341 (2018) 126–136, <https://doi.org/10.1016/j.cej.2018.01.136>.
- [3] K. Zhang, Y. Xue, J. Zhang, X. Hu, Removal of lead from acidic wastewater by biomineralized bacteria with pH self-regulation, *Chemosphere* 241 (2020), 125041, <https://doi.org/10.1016/j.chemosphere.2019.125041>.
- [4] Z. Lv, X. Tan, C. Wang, A. Alsaedi, T. Hayat, C. Chen, Metal-organic frameworks-derived 3D yolk shell-like structure Ni@carbon as a recyclable catalyst for Cr(VI) reduction, *Chem. Eng. J.* 389 (2020), 123428, <https://doi.org/10.1016/j.cej.2019.123428>.
- [5] X.-D. Du, X.-H. Yi, P. Wang, W. Zheng, J. Deng, C.-C. Wang, Robust photocatalytic reduction of Cr(VI) on UiO-66-NH<sub>2</sub>(Zr/Hf) metal-organic framework membrane under sunlight irradiation, *Chem. Eng. J.* 356 (2019) 393–399, <https://doi.org/10.1016/j.cej.2018.09.084>.
- [6] Z. Shi, Y. Zhang, X. Shen, G. Duoerkun, B. Zhu, L. Zhang, M. Li, Z. Chen, Fabrication of g-C<sub>3</sub>N<sub>4</sub>/BiOBr heterojunctions on carbon fibers as weavable photocatalyst for degrading tetracycline hydrochloride under visible light, *Chem. Eng. J.* 386 (2020), 124010, <https://doi.org/10.1016/j.cej.2020.124010>.
- [7] L. Zeng, S. Li, X. Li, J. Li, S. Fan, X. Chen, Z. Yin, M. Tade, S. Liu, Visible-light-driven sonophotocatalysis and peroxymonosulfate activation over 3D urchin-like MoS<sub>2</sub>/C nanoparticles for accelerating levofloxacin elimination: Optimization and kinetic study, *Chem. Eng. J.* 378 (2019), 122039, <https://doi.org/10.1016/j.cej.2019.122039>.
- [8] G. Duoerkun, Y. Zhang, Z. Shi, X. Shen, W. Cao, T. Liu, J. Liu, Q. Chen, L. Zhang, Construction of n-TiO<sub>2</sub>/p-Ag<sub>2</sub>O junction on carbon fiber cloth with vis–nir photoresponse as a filter-membrane-shaped photocatalyst, *Adv. Fiber Mater.* 2 (1) (2020) 13–23, <https://doi.org/10.1007/s42765-019-00025-8>.

- [9] T. Hou, Q. Li, Y. Zhang, W. Zhu, K. Yu, S. Wang, Q. Xu, S. Liang, L. Wang, Near-infrared light-driven photofixation of nitrogen over  $\text{Ti}_3\text{C}_2\text{Tx}/\text{TiO}_2$  hybrid structures with superior activity and stability, *Appl. Catal. B: Environ.* 273 (2020), 119072, <https://doi.org/10.1016/j.apcatb.2020.119072>.
- [10] M. Abinaya, K. Govindan, M. Kalpana, K. Saravanakumar, S.L. Prabavathi, V. Muthuraj, A. Jang, Reduction of hexavalent chromium and degradation of tetracycline using a novel indium-doped  $\text{Mn}_2\text{O}_3$  nanorod photocatalyst, *J. Hazard. Mater.* 397 (2020), 122885, <https://doi.org/10.1016/j.jhazmat.2020.122885>.
- [11] J. Liu, H. Lin, Y. He, Y. Dong, E.R.G.Y. Menzembere, Novel  $\text{CoS}_2/\text{MoS}_2$ /Zeolite with excellent adsorption and photocatalytic performance for tetracycline removal in simulated wastewater, *J. Clean. Prod.* 260 (2020), 121047, <https://doi.org/10.1016/j.jclepro.2020.121047>.
- [12] B. Xia, F. Deng, S. Zhang, L. Hua, X. Luo, M. Ao, Design and synthesis of robust Z-scheme  $\text{ZnS-SnS}_2$  n-n heterojunctions for highly efficient degradation of pharmaceutical pollutants: performance, valence/conduction band offset photocatalytic mechanisms and toxicity evaluation, *J. Hazard. Mater.* 392 (2020), 122345, <https://doi.org/10.1016/j.jhazmat.2020.122345>.
- [13] S. Raha, M. Ahmaruzzaman, Enhanced performance of a novel superparamagnetic  $\text{g-C}_3\text{N}_4/\text{NiO}/\text{ZnO}/\text{Fe}_3\text{O}_4$  nanohybrid photocatalyst for removal of esomeprazole: Effects of reaction parameters, co-existing substances and water matrices, *Chem. Eng. J.* 395 (2020), 124969, <https://doi.org/10.1016/j.cej.2020.124969>.
- [14] S. Adhikari, S. Mandal, D.-H. Kim, Z-scheme 2D/1D  $\text{MoS}_2$  nanosheet-decorated  $\text{Ag}_2\text{Mo}_2\text{O}_7$  microrods for efficient catalytic oxidation of levofloxacin, *Chem. Eng. J.* 373 (2019) 31–43, <https://doi.org/10.1016/j.cej.2019.05.017>.
- [15] T. Li, Y. Gao, L. Zhang, X. Xing, X. Huang, F. Li, Y. Jin, C. Hu, Enhanced Cr(VI) reduction by direct transfer of photo-generated electrons to Cr 3d orbitals in  $\text{CrO}_4^{2-}$  intercalated BiOBr with exposed (110) facets, *Appl. Catal. B: Environ.* 277 (2020), 119065, <https://doi.org/10.1016/j.apcatb.2020.119065>.
- [16] M. Ratova, J. Redfern, J. Verran, P.J. Kelly, Highly efficient photocatalytic bismuth oxide coatings and their antimicrobial properties under visible light irradiation, *Appl. Catal. B: Environ.* 239 (2018) 223–232, <https://doi.org/10.1016/j.apcatb.2018.08.020>.
- [17] Z. Li, H. Yang, L. Zhang, R. Liu, Y. Zhou, Stainless steel mesh-supported three-dimensional hierarchical  $\text{SnO}_2/\text{Zn}_2\text{SnO}_4$  composite for the applications in solar cell, gas sensor, and photocatalysis, *Appl. Surf. Sci.* 502 (2020), 144113, <https://doi.org/10.1016/j.apsusc.2019.144113>.
- [18] H. Zhao, L. Zhang, X. Gu, S. Li, B.o. Li, H. Wang, J. Yang, J. Liu,  $\text{Fe}_2\text{O}_3$ -AgBr nonwoven cloth with hierarchical nanostructures as efficient and easily recyclable macroscale photocatalysts, *RSC Adv.* 5 (15) (2015) 10951–10959, <https://doi.org/10.1039/C4RA13254H>.
- [19] S. Li, L. Zhang, H. Wang, Z. Chen, J. Hu, K. Xu, J. Liu,  $\text{Ta}_3\text{N}_5$ -Pt nonwoven cloth with hierarchical nanopores as efficient and easily recyclable macroscale photocatalysts, *Sci. Rep.* 4 (2014) 3978, <https://doi.org/10.1038/srep03978>.
- [20] Y. Zhang, G. Duoerkun, Z. Shi, W. Cao, T. Liu, J. Liu, L. Zhang, M. Li, Z. Chen, Construction of  $\text{TiO}_2/\text{Ag}_3\text{PO}_4$  nanojunctions on carbon fiber cloth for photocatalytically removing various organic pollutants in static or flowing wastewater, *J. Colloid Interface Sci.* 571 (2020) 213–221, <https://doi.org/10.1016/j.jcis.2020.03.049>.
- [21] L.i. Luo, X. Shen, L. Song, Y. Zhang, B.o. Zhu, J. Liu, Q. Chen, Z. Chen, L. Zhang,  $\text{MoS}_2/\text{Bi}_2\text{S}_3$  heterojunctions-decorated carbon-fiber cloth as flexible and filter-membrane-shaped photocatalyst for the efficient degradation of flowing wastewater, *J. Alloy. Compd.* 779 (2019) 599–608, <https://doi.org/10.1016/j.jallcom.2018.11.154>.
- [22] S. Li, J. Cui, X. Wu, X. Zhang, Q.i. Hu, X. Hou, Rapid in situ microwave synthesis of  $\text{Fe}_3\text{O}_4$ @ $\text{MIL-100}(\text{Fe})$  for aqueous diclofenac sodium removal through integrated adsorption and photodegradation, *J. Hazard. Mater.* 373 (2019) 408–416, <https://doi.org/10.1016/j.jhazmat.2019.03.102>.
- [23] M. Alvaro, E. Carbonell, B. Ferrer, F. LlabrésXamena, H. Garcia, Semiconductor Behavior of a Metal-Organic Framework (MOF), *Chem. Eur. J.* 13 (18) (2007) 5106–5112, <https://doi.org/10.1002/chem.200601003>.
- [24] J.H. Cavka, S. Jakobsen, U. Olsbye, N. Guillou, C. Lamberti, S. Bordiga, K. P. Lillerud, A new zirconium inorganic building brick forming metal organic frameworks with exceptional stability, *J. Am. Chem. Soc.* 130 (42) (2008) 13850–13851, <https://doi.org/10.1021/ja8057953>.
- [25] L. Shen, W. Wu, R. Liang, R. Lin, L. Wu, Highly dispersed palladium nanoparticles anchored on  $\text{UiO-66}(\text{NH}_2)$  metal-organic framework as a reusable and dual functional visible-light-driven photocatalyst, *Nanoscale* 5 (19) (2013) 9374, <https://doi.org/10.1039/c3nr03153e>.
- [26] Y. Pan, X. Yuan, L. Jiang, H. Wang, H. Yu, J. Zhang, Stable self-assembly  $\text{AgI}/\text{UiO-66}(\text{NH}_2)$  heterojunction as efficient visible-light responsive photocatalyst for tetracycline degradation and mechanism insight, *Chem. Eng. J.* 384 (2020), 123310, <https://doi.org/10.1016/j.cej.2019.123310>.
- [27] N. Liu, W. Huang, M. Tang, C. Yin, B. Gao, Z. Li, L. Tang, J. Lei, L. Cui, X. Zhang, In-situ fabrication of needle-shaped  $\text{MIL-53}(\text{Fe})$  with  $1\text{T-MoS}_2$  and study on its enhanced photocatalytic mechanism of ibuprofen, *Chem. Eng. J.* 359 (2019) 254–264, <https://doi.org/10.1016/j.cej.2018.11.143>.
- [28] J. Qiu, X. Zhang, K. Xie, X.-F. Zhang, Y.i. Feng, M. Jia, J. Yao, Noble metal nanoparticle-functionalized Zr-metal organic frameworks with excellent photocatalytic performance, *J. Colloid Interface Sci.* 538 (2019) 569–577, <https://doi.org/10.1016/j.jcis.2018.12.024>.
- [29] X. Hu, S. Lu, J. Tian, N. Wei, X. Song, X. Wang, H. Cui, The selective deposition of  $\text{MoS}_2$  nanosheets onto (101) facets of  $\text{TiO}_2$  nanosheets with exposed (001) facets and their enhanced photocatalytic  $\text{H}_2$  production, *Appl. Catal. B: Environ.* 241 (2019) 329–337, <https://doi.org/10.1016/j.apcatb.2018.09.051>.
- [30] S. Subudhi, G. Swain, S.P. Tripathy, K. Parida,  $\text{UiO-66-NH}_2$  metal-organic frameworks with embedded  $\text{MoS}_2$  nanoflakes for visible-light-mediated  $\text{H}_2$  and  $\text{O}_2$  evolution, *Inorg. Chem.* 59 (14) (2020) 9824–9837, <https://doi.org/10.1021/acs.inorgchem.0c01030.s001>.
- [31] Y. Zhang, L.i. Luo, Z. Shi, X. Shen, C. Peng, J. Liu, Z. Chen, Q. Chen, L. Zhang, Synthesis of  $\text{MoS}_2/\text{CdS}$  heterostructures on carbon-fiber cloth as filter-membrane-shaped photocatalyst for purifying the flowing wastewater under visible-light illumination, *ChemCatChem* 11 (12) (2019) 2855–2863, <https://doi.org/10.1002/cctc.201900542>.
- [32] S. Wan, M. Ou, Q. Zhong, X. Wang, Perovskite-type  $\text{CsPbBr}_3$  quantum dots/ $\text{UiO-66}(\text{NH}_2)$  nanojunction as efficient visible-light-driven photocatalyst for  $\text{CO}_2$  reduction, *Chem. Eng. J.* 358 (2019) 1287–1295, <https://doi.org/10.1016/j.cej.2018.10.120>.
- [33] Z. Shi, P. Xu, X. Shen, Y. Zhang, L.i. Luo, G. Duoerkun, L. Zhang,  $\text{TiO}_2/\text{MoS}_2$  heterojunctions-decorated carbon fibers with broad-spectrum response as weavable photocatalyst/photocatalyst, *Mater. Res. Bull.* 112 (2019) 354–362, <https://doi.org/10.1016/j.materresbull.2019.01.005>.
- [34] F. Guo, X. Huang, Z. Chen, H. Ren, M. Li, L. Chen,  $\text{MoS}_2$  nanosheets anchored on porous  $\text{ZnSnO}_3$  cubes as an efficient visible-light-driven composite photocatalyst for the degradation of tetracycline and mechanism insight, *J. Hazard. Mater.* 390 (2020), 122158, <https://doi.org/10.1016/j.jhazmat.2020.122158>.
- [35] X. Wang, X. Zhao, D. Zhang, G. Li, H. Li, Microwave irradiation induced  $\text{UiO-66-NH}_2$  anchored on graphene with high activity for photocatalytic reduction of  $\text{CO}_2$ , *Appl. Catal. B: Environ.* 228 (2018) 47–53, <https://doi.org/10.1016/j.apcatb.2018.01.066>.
- [36] A. Wang, Z. Zheng, H. Wang, Y. Chen, C. Luo, D. Liang, B. Hu, R. Qiu, K. Yan, 3D hierarchical  $\text{H}_2$ -reduced Mn-doped  $\text{CeO}_2$  microflowers assembled from nanotubes as a high-performance Fenton-like photocatalyst for tetracycline antibiotics degradation, *Appl. Catal. B: Environ.* 277 (2020), 119171, <https://doi.org/10.1016/j.apcatb.2020.119171>.
- [37] P. Xu, X. Shen, L. Luo, Z. Shi, Z. Liu, Z. Chen, M. Zhu, L. Zhang, Preparation of  $\text{TiO}_2/\text{Bi}_2\text{WO}_6$  nanostructured heterojunctions on carbon fibers as a weavable visible-light photocatalyst/photocatalyst, *Environ. Sci. Nano* 5 (2018) 327–337, <https://doi.org/10.1039/c7en00822h>.
- [38] Y. Li, B. Sun, H. Lin, Q. Ruan, Y. Geng, J. Liu, H. Wang, Y. Yang, L. Wang, K.C. Tam, Efficient visible-light induced  $\text{H}_2$  evolution from  $\text{T-Cd}_x\text{Zn}_{1-x}\text{S}/\text{defective MoS}_2$  nanohybrid with both bulk twinning homojunctions and interfacial heterostructures, *Appl. Catal. B: Environ.* 267 (2020), 118702, <https://doi.org/10.1016/j.apcatb.2020.118702>.
- [39] Y. Zhang, L. Wang, S. Park, X. Kong, X. Lan, Z. Song, J. Shi, Single near-infrared-laser driven Z-scheme photocatalytic  $\text{H}_2$  evolution on upconversion material/ $\text{Ag}_3\text{PO}_4$ @black phosphorus, *Chem. Eng. J.* 375 (2019), 121967, <https://doi.org/10.1016/j.cej.2019.121967>.
- [40] S. Bolar, S. Shit, J.S. Kumar, N.C. Murmu, R.S. Ganesh, H. Inokawa, T. Kaila, Optimization of active surface area of flower like  $\text{MoS}_2$  using V-doping towards enhanced hydrogen evolution reaction in acidic and basic medium, *Appl. Catal. B: Environ.* 254 (2019) 432–442, <https://doi.org/10.1016/j.apcatb.2019.04.028>.
- [41] Y. Zhang, W. Cui, W. An, L. Liu, Y. Liang, Y. Zhu, Combination of photoelectrocatalysis and adsorption for removal of bisphenol A over  $\text{TiO}_2$ -graphene hydrogel with 3D network structure, *Appl. Catal. B: Environ.* 221 (2018) 36–46, <https://doi.org/10.1016/j.apcatb.2017.08.076>.
- [42] J. Zhou, W. Liu, W. Cai, The synergistic effect of  $\text{Ag}/\text{AgCl}/\text{ZIF-8}$  modified  $\text{g-C}_3\text{N}_4$  composite and peroxymonosulfate for the enhanced visible-light photocatalytic degradation of levofloxacin, *Sci. Total Environ.* 696 (2019), 133962, <https://doi.org/10.1016/j.scitotenv.2019.133962>.
- [43] L. Li, C. Niu, H. Guo, J. Wang, M. Ruan, L. Zhang, C. Liang, H. Liu, Y. Yang, Efficient degradation of levofloxacin with magnetically separable  $\text{ZnFe}_2\text{O}_4/\text{NCDs}/\text{Ag}_2\text{CO}_3$  Z-scheme heterojunction photocatalyst: Vis-NIR light response ability and mechanism insight, *Chem. Eng. J.* 383 (2020), 123192, <https://doi.org/10.1016/j.cej.2019.123192>.
- [44] L. Shen, S. Liang, W. Wu, R. Liang, L. Wu, Multifunctional  $\text{NH}_2$ -mediated zirconium metal-organic framework as an efficient visible-light-driven photocatalyst for selective oxidation of alcohols and reduction of aqueous Cr(VI), *Dalton Trans.* 42 (37) (2013) 13649, <https://doi.org/10.1039/c3dt51479j>.
- [45] C. Liang, C. Niu, L. Zhang, X. Wen, S. Yang, H. Guo, G. Zeng, Construction of 2D heterojunction system with enhanced photocatalytic performance: Plasmonic Bi and reduced graphene oxide co-modified  $\text{Bi}_5\text{O}_7\text{I}$  with high-speed charge transfer channels, *J. Hazard. Mater.* 361 (2019) 245–258, <https://doi.org/10.1016/j.jhazmat.2018.08.099>.
- [46] R. Liang, L. Shen, F. Jing, W. Wu, N. Qin, R. Lin, L. Wu,  $\text{NH}_2$ -mediated indium metal-organic framework as a novel visible-light-driven photocatalyst for reduction of the aqueous Cr(VI), *Appl. Catal. B: Environ.* 162 (2015) 245–251, <https://doi.org/10.1016/j.apcatb.2014.06.049>.
- [47] S.G. Fard, M. Haghghi, M. Shabani, Facile one-pot ultrasound-assisted solvothermal fabrication of ball-flowerlike nanostructured  $(\text{BiOBr})_x(\text{Bi}_2\text{O}_3)_{(1-x)}$  solid-solution for high active photodegradation of antibiotic levofloxacin under sun-light, *Appl. Catal. B: Environ.* 248 (2019) 320–331, <https://doi.org/10.1016/j.apcatb.2019.02.021>.
- [48] N. Samsandee, S. Phatanasri, P. Ramakul, U. Pancharoen, Thermodynamic parameters and isotherm application on enantiomeric separation of levofloxacin using hollow fiber supported liquid membrane system, *Sep. Purif. Technol.* 195 (2018) 377–387, <https://doi.org/10.1016/j.seppur.2017.12.034>.
- [49] M. Zhang, C. Lai, B. Li, D. Huang, G. Zeng, P. Xu, L. Qin, S. Liu, X. Liu, H. Yi, M. Li, C. Chu, Z. Chen, Rational design 2D/2D  $\text{BiOBr}/\text{CDs}/\text{g-C}_3\text{N}_4$  Z-scheme heterojunction photocatalyst with carbon dots as solid-state electron mediators for enhanced visible and NIR photocatalytic activity: Kinetics, intermediates, and mechanism insight, *J. Catal.* 369 (2019) 469–481, <https://doi.org/10.1016/j.jcat.2018.11.029>.